



# Thermal shock and fatigue resistance of tungsten materials under transient heat loading



Xiaoxin Zhang<sup>a</sup>, Qingzhi Yan<sup>a,\*</sup>, Shaoting Lang<sup>a</sup>, Min Xia<sup>a</sup>, Xiang Liu<sup>b</sup>, Changchun Ge<sup>a</sup>

<sup>a</sup> Institute of Nuclear Materials, University of Science and Technology Beijing, 100083 Beijing, PR China

<sup>b</sup> Southwestern Institute of Physics, P.O. Box 432, 610041 Chengdu, PR China

## HIGHLIGHTS

- Basic properties, thermal load resistance of PW, WL10 and W-K were characterized.
- DBTT values were 823–873, 723–773 and 873 K for PW, WL10 and W-K.
- Coarse La<sub>2</sub>O<sub>3</sub> at the grain boundary reduced the thermal load resistance of WL10.
- Fine K bubbles at the grain boundary improved the thermal load resistance of W-K.

## ARTICLE INFO

### Article history:

Available online 8 August 2014

## ABSTRACT

Transient heat loading tests were performed on rolled pure tungsten (PW) and lanthanum oxide doped tungsten (WL10) as well as swaged + rolled potassium doped tungsten (W-K) samples using an electron beam. In thermal shock tests, the cracking threshold was 0.44–0.66, 0.17–0.22 and 0.44–0.66 GW/m<sup>2</sup> for PW, WL10 and W-K, respectively. The melting threshold was over 1.1 GW/m<sup>2</sup> for PW and W-K while 0.66–0.88 GW/m<sup>2</sup> for WL10. In thermal fatigue tests, the obvious roughening threshold was over 1000 cycles for PW and WL10 while 1–100 cycles for W-K. The cracking threshold was 100–1000 cycles for PW, 1–100 cycles for WL10 and over 1000 cycles for W-K alloy. WL10 displayed worse thermal and fatigue resistance while W-K exhibited better properties compared with PW, which was attributed to differences in thermal–mechanical properties of the three tungsten alloys, in addition to the size and number density of La<sub>2</sub>O<sub>3</sub> particles and potassium bubbles.

© 2014 Elsevier B.V. All rights reserved.

## 1. Introduction

Tungsten (W) is a prime candidate for the plasma facing material (PFM) in future fusion reactors. The PFM will be exposed to steady-state heat loads and several types of transient heat loads [1–4]. These intense heat loads may result in cracks, surface melting, evaporation, droplet ejection and fatigue fracture, which may cause fatal destruction of the PFM and plasma contamination. Therefore, it is important to assess the thermal shock and fatigue resistance of tungsten.

However, some researchers have reported that tungsten itself is not completely suitable for PFM. By contrast, lanthanum oxide doped tungsten (W–La<sub>2</sub>O<sub>3</sub>) and potassium doped tungsten (W-K) exhibit better thermal–mechanical properties than pure tungsten (PW). Mabuchi et al. found that the annealed W–La<sub>2</sub>O<sub>3</sub> exhibited

higher strength than the annealed pure tungsten in the temperature range of 1273–1973 K [5]. Kim [6] reported that the La<sub>2</sub>O<sub>3</sub> particles can act as inhibitors to consolidation in the sintering process regardless of oxide contents during sintering process and act to strengthen the W–La<sub>2</sub>O<sub>3</sub> composite when the oxide content is below 2 wt%. In addition, a dispersion of oxide nano-particles in tungsten could provide a large amount of interfacial regions, which may act as sinks for irradiation-induced point defects and improve the irradiation resistance [7]. In the case of W-K, the potassium bubbles were thought to increase the recrystallization temperature and high temperature creep properties. W-K alloys showed higher fracture toughness than pure tungsten in the sintered (measured by disk shaped compact tension test) and rolled states (measured by single edge notched bend test) [8].

More importantly, plastic deformation combined with appropriate heat treatment is another useful method to improve the mechanical properties of tungsten, which has been widely clarified by experimental studies. For example, Yan [9] indicated that the ductile–brittle transition temperature (DBTT) of tungsten could

\* Corresponding author. Address: Institute of Nuclear Materials, University of Science & Technology Beijing, 30 Xueyuan Road, Haidian District, Beijing, PR China. Tel./fax: +86 01062334951.

E-mail address: [qzyan@ustb.edu.cn](mailto:qzyan@ustb.edu.cn) (Q. Yan).

**Table 1**

Chemical compositions of the pure tungsten powder and potassium doped tungsten powder, PPM.

<i>Pure tungsten powder</i>
O < 350, C < 25, Mo < 14, Fe < 12, Cr < 10, K < 7, Ca < 6, As < 6, Si < 6, S < 5, Na < 5, P < 5, Mg < 2, Al < 2, Sb < 2, V < 2, Mn < 2, Ti < 2, Co < 2, Sn < 1, Bi < 1, Cd < 1, Pb < 1, Cu < 1
<i>Potassium doped tungsten powder</i>
K < 1700, Al < 150, Si < 2500, O < 3000, Fe < 13, Mo < 25, As < 8, Mn < 8, Ni < 7, Ca < 5, Ti < 5, Mg < 3, Na < 3, V < 3, Cr < 2, Bi < 1, Cd < 1, Co < 1, Cu < 1, Pb < 1, Sb < 2, Sn < 1

be reduced by adding  $\text{La}_2\text{O}_3$  and using a swaging + rolling process. In addition, Wei and Kecskes [10] found that rolling below the nominal recrystallization temperature 1523 K concomitantly enhanced the ductility and strength of tungsten.

Therefore, W- $\text{La}_2\text{O}_3$  and W-K with deformed microstructures might exhibit acceptable thermal shock and fatigue resistance and should be systematically investigated. In this paper, PW and W-1 wt%  $\text{La}_2\text{O}_3$  (WL10) bulk alloys were prepared by rolling and W-K alloy was manufactured via rolling + swaging.

## 2. Experiments

The starting tungsten powders were commercial. The grain size of the pure tungsten powder was about 3  $\mu\text{m}$ . The chemical compositions of the pure tungsten powder are shown in Table 1. W- $\text{La}_2\text{O}_3$  powder was prepared by mechanical alloying using the pure tungsten powder mentioned above and commercial  $\text{La}_2\text{O}_3$  powder as the starting materials. The grain size of the potassium doped tungsten powder was around 3.5  $\mu\text{m}$  and the chemical compositions were presented in Table 1 as well. Then the pure tungsten powder and the doped tungsten powders were pressed to about 55% of the theoretical density, presintered at about 1473 K for 40 min and sintered at high temperature (about 2373 K, 2 h for PW, WL10 and about 3073 K, 15 min for W-K) to achieve the densification of the billet. Subsequently, the PW samples were rolled from 30-mm-thick to 12 mm with an engineering strain of 60%. The sintered WL10 billets were rolled from 25-mm-thick to 12 mm with an engineering strain of 52%. For W-K, sintered rods of W doped with 70–75 ppm K were swaged from 15 mm-diameter to 9 mm at 1873 K, subsequently annealed at 2373 K for 1 h

under hydrogen atmosphere to improve the deformability, then the swaged rods were cut into 8 mm-thick-plates and rolled to 3 mm thickness. Finally, these deformed sheets were annealed at 1373 K in hydrogen atmosphere for 2 h to relax residual stresses. For PW and WL10, the grain orientation was parallel to the heat transfer direction. For W-K, the grain orientation was perpendicular to the heat transfer direction due to the size limitation of the deformed bulk sample (only 3 mm thickness).

The detailed parameters for the transient high heat load tests were described in Ref. [11] and the thermal shock and high heat flux tests were performed on plates of each material having dimensions  $12 \times 12 \times 3 \text{ mm}^3$ . A homogeneous heat load distribution in the  $4 \times 4 \text{ mm}^2$  beam spot was achieved by fast scanning (10 kHz) of the electron beam. Thermal shock tests were performed at absorbed power densities that ranged from 0.22 to 1.1  $\text{GW/m}^2$  with an increment of 0.22  $\text{GW/m}^2$  with just 1 pulse with pulse duration of 5 ms. The thermal fatigue tests were carried out with 1, 100, and 1000 pulses at an absorbed power density of 0.25  $\text{GW/m}^2$  for PW, 0.17  $\text{GW/m}^2$  for WL10 and 0.44  $\text{GW/m}^2$  for W-K, respectively. Fig. 1 shows the surface temperatures of different tungsten grades in thermal shock and fatigue tests. The surface temperatures showed a general increase with absorbed power density. WL10 exhibited the highest surface temperature among these three tungsten grades since it had the lowest thermal conductivity of 140.1 W/mK.

Microstructures were observed via optical microscopy and scanning electron microscopy (SEM) and field emission scanning electron microscopy (FESEM) as well as transmission electron microscopy (TEM). Vickers micro-hardness tests were performed under a load of 1.96 N for 10 s. Density was measured using Archimedes' method. Three point bending (3 PB) specimens of  $37 \times 4 \times 3 \text{ mm}^3$  were produced to measure the fracture strength. For Charpy impact tests, specimens with dimensions of  $27 \times 4 \times 3 \text{ mm}^3$ , a notch depth of 1 mm and a notch root radius of 0.1 mm were prepared. The specimens were heated to 673–1273 K in argon atmosphere, then moved to the test fixture located outside the furnace and hit by a striker (25 J) immediately. The thermal conductivity was calculated by the following formula:

$$k = \rho \cdot c_p \cdot \alpha$$

where  $k$  is the thermal conductivity,  $\rho$  is bulk density,  $c_p$  is specific heat,  $\alpha$  is the thermal diffusivity. The specific heat was measured by a thermal analyzing apparatus (Dupont 1090B, America). The

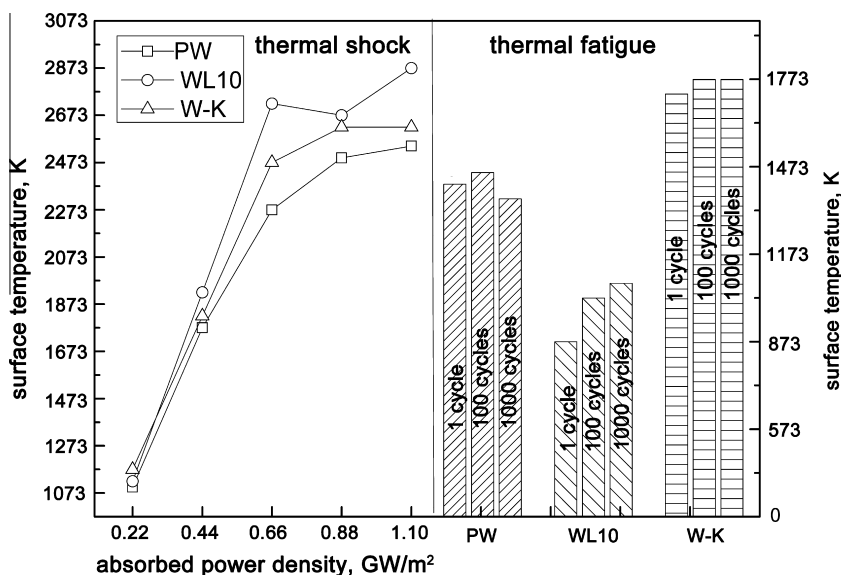


Fig. 1. Surface temperatures of tungsten grades in thermal shock and fatigue tests.

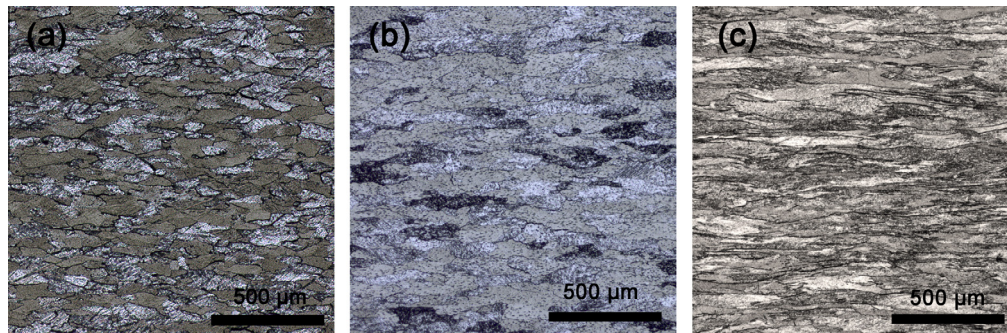


Fig. 2. Microstructures on the cross-section surfaces of the three tungsten grades: (a) PW; (b) WL10; (c) W-K.

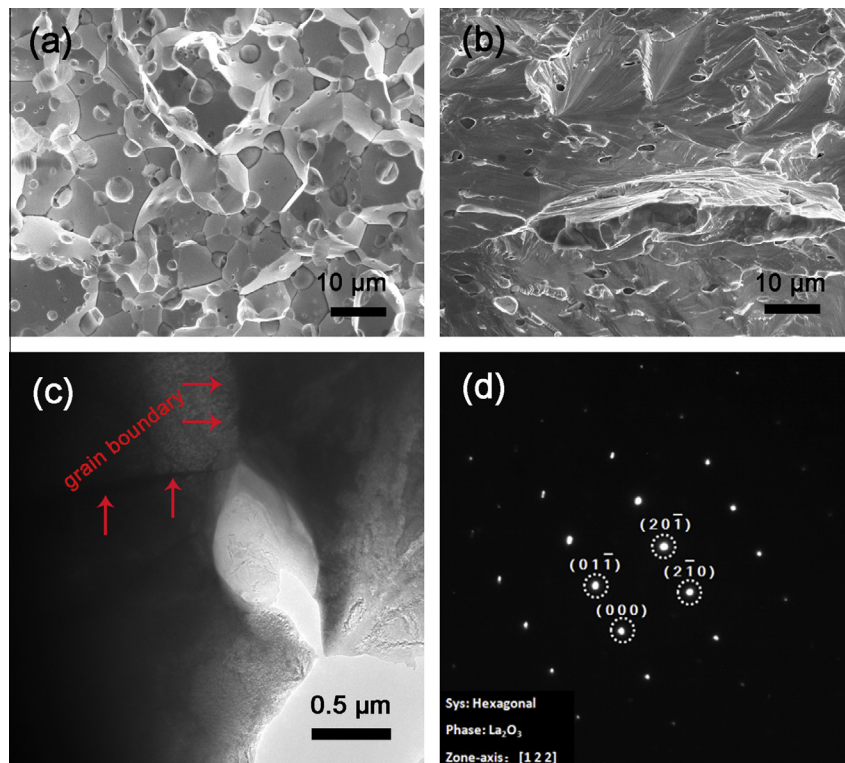


Fig. 3.  $\text{La}_2\text{O}_3$  particles distributed in the tungsten matrix: (a) sintered tungsten, fracture morphology, SEM; (b) rolled tungsten, fracture morphology, SEM; (c) rolled tungsten, TEM; (d) electron diffraction pattern of the white particle in (c).

thermal diffusivity was determined using a laser flash apparatus (LFA 457, Germany).

### 3. Results and discussion

#### 3.1. Basic properties

Fig. 2 shows the microstructures of the cross-section surfaces of these three tungsten grades. For W-K, the grains were elongated along the rolling direction with the biggest aspect ratio of roughly 10:1 (Fig. 2(c)), the aspect ratio decreased to around 5:1 for PW (Fig. 2(a)). In the case of WL10, the aspect ratio further decreased to 3.5:1 (Fig. 2(b)), which was due to the reduced deformation for this alloy and higher rolling temperature. Fig. 3 shows the  $\text{La}_2\text{O}_3$  particles distributed in the tungsten matrix. The spherical  $\text{La}_2\text{O}_3$  particles with a size of 1–3  $\mu\text{m}$  distributed at the grain boundary of the sintered tungsten sample and the grain size of the tungsten was about 15  $\mu\text{m}$  (Fig. 3(a)). After rolling, ellipsoid

$\text{La}_2\text{O}_3$  particles with an aspect ratio of roughly 1.5–3 were detected on the fracture surface (Fig. 3(b)). The length of the ellipsoid  $\text{La}_2\text{O}_3$  particle was around 1–4  $\mu\text{m}$ . Fig. 3(c) shows the TEM image of the  $\text{La}_2\text{O}_3$  particles distributed at the grain boundary, the grain boundaries have been noted by the arrows. The aspect ratio of this  $\text{La}_2\text{O}_3$  particle was about 1.5 ( $\approx 1000 \text{ nm} : 650 \text{ nm}$ ). Fig. 3(d) shows the electron diffraction pattern of the white particle in Fig. 3(c) to confirm that this particle was  $\text{La}_2\text{O}_3$ , and this electron diffraction pattern was in agreement with the standard electron diffraction pattern of the hexagonal  $\text{La}_2\text{O}_3$ . The  $\text{La}_2\text{O}_3$  particle number density (per unit area) was about  $10^8 \text{ m}^{-2}$  according to Fig. 3 (b), assuming that the fracture surface was flat. So we concluded that a moderate quantity of ellipsoid  $\text{La}_2\text{O}_3$  particles with an aspect ratio of roughly 1.5–3, length of 1–4  $\mu\text{m}$  and number density (per unit area) of  $10^8 \text{ m}^{-2}$  distributed at the grain boundaries. Fig. 4(a) and (b) show the fracture morphology of the rolled potassium doped tungsten by FESEM. A large amount of potassium bubbles were detected on the intergranular fracture surface and the maximum diameter of the bubble was about 200 nm. Whereas no potassium bubble



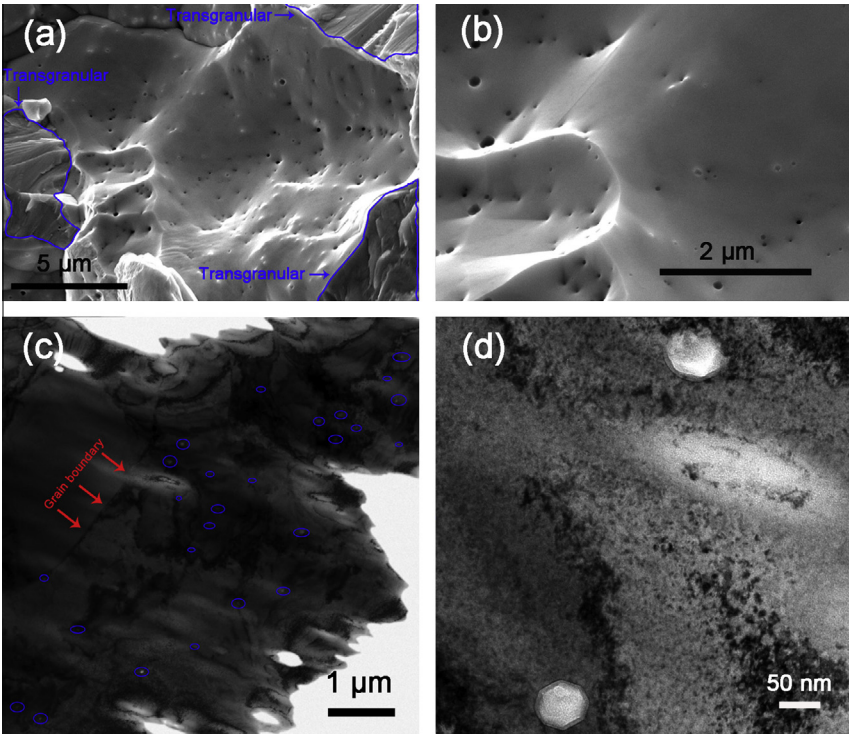


**Fig. 4.** Potassium bubbles distributed in the rolled potassium doped tungsten matrix: (a) fracture morphology, FESEM, low-magnification image; (b) fracture morphology, FESEM, high-magnification image; (c) TEM, low-magnification image; (d) TEM, high-magnification image.

**Table 2**  
Thermal-mechanical properties of different tungsten grades.

Sample	PW	WL10	W-K
State	Rolling	Rolling	Swaging + rolling
Deformation degree (%)	60	52	64 for swaging, 62.5 for rolling
Relative density (%)	98.4	97.2	98.2
Micro-hardness (HV <sub>0.2</sub> )	436	452	427
Bending strength (MPa)	1068	1312	856
DBTT (K)	823–873	723–773	873
Thermal conductivity (W/m K)	175.6	140.1	159.1

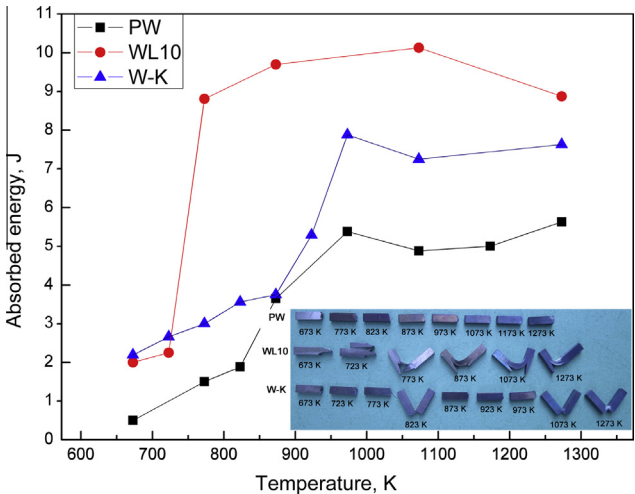


**Fig. 5.** Results of the Charpy impact tests.

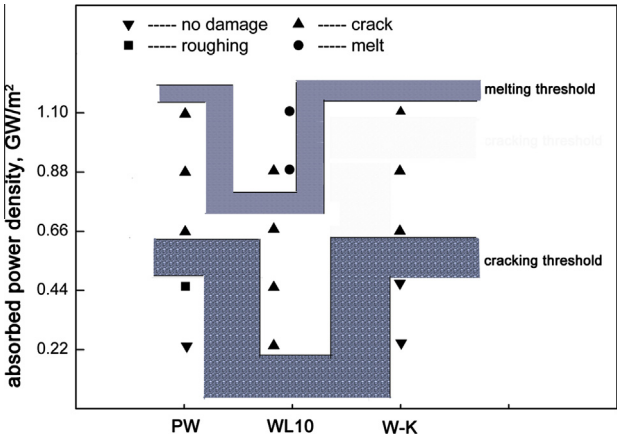


**Fig. 6.** Surface modifications after thermal shock tests in different tungsten grades.

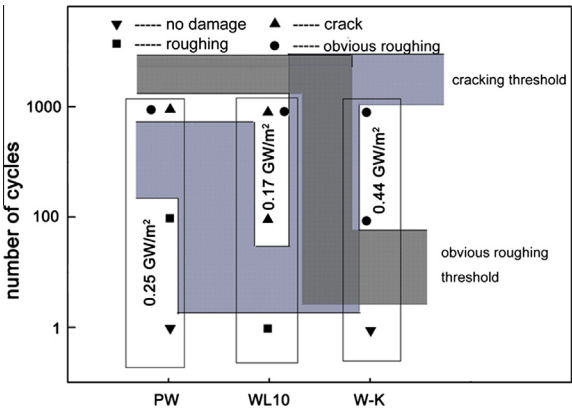


**Fig. 7.** Surface modifications after thermal fatigue tests in different tungsten grades.

formed on the transgranular fracture surface noted by the blue arrows in Fig. 4(a). So we concluded that the potassium bubbles existed at the grain boundaries. Fig. 4(c) shows TEM images of the potassium bubbles distributed in the tungsten matrix. The potassium bubble number density (per unit area) was about  $10^{13} \text{ m}^{-2}$  according to Fig. 4(b), assuming that the fracture surface was flat. Fig. 4(d) shows the high-magnification TEM image of the rolled potassium doped tungsten and the size of the bubbles was about 50 nm. So we concluded that bubbles with sizes of 50–200 nm and number density (per unit area) of  $10^{13} \text{ m}^{-2}$  were distributed at the grain boundaries. Table 2 presents the thermal–mechanical properties of the different tungsten grades. WL10 exhibited the highest micro-hardness (452 HV<sub>0.2</sub>) and bending strength (1312 MPa). Fig. 5 shows the results of the Charpy impact tests, the absorbed energy for WL10 was almost the highest among the three tungsten grades tested at the same temperatures.

PW specimens fractured completely within the whole test temperature range. WL10 specimens showed delamination (fractures propagate parallel to the specimen's long side and perpendicular to the notch) at temperatures varied from 773 K to 1273 K. In the case of W-K, samples fractured completely at 673–773 K and ductile fracture observed at 1073–1273 K. In summary, there are three types of fracture: brittle, delamination, and ductile. The brittle-to-delamination transition temperature (defined in analogy to DBTT) was 723–773 K for WL10 while the DBTT was 823–873 K for PW and  $\sim 873 \text{ K}$  for W-K.

### 3.2. Thermal shock test

Thermal shock tests were performed on PW, WL10 and W-K grades with different absorbed power densities of 0.22, 0.44, 0.66, 0.88 and  $1.1 \text{ GW/m}^2$ . Fig. 6 shows surface modifications after

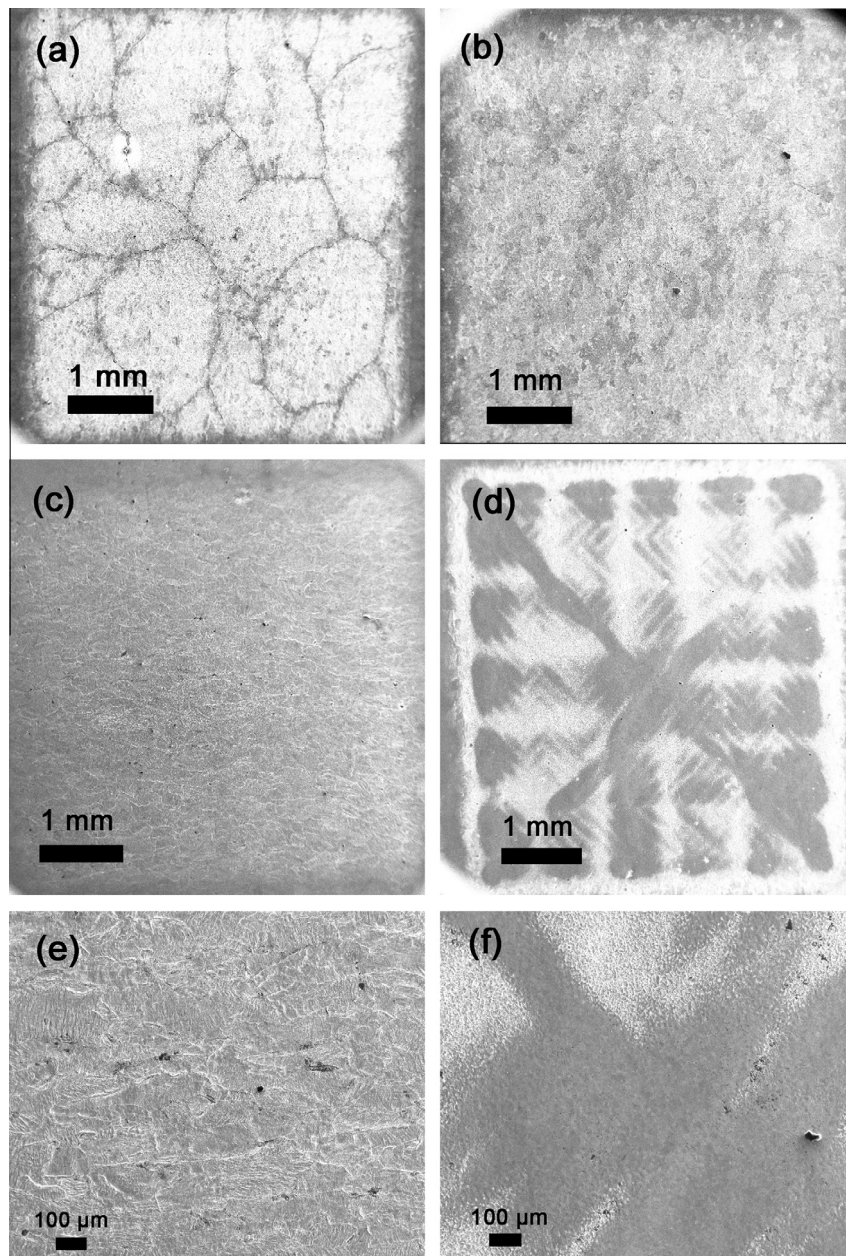


**Fig. 8.** SEM images of tungsten grades after thermal fatigue tests. Low-magnification: (a) PW,  $0.25 \text{ GW/m}^2$ , 1000 cycles; (b) WL10,  $0.17 \text{ GW/m}^2$ , 1000 cycles; (c) W-K,  $0.44 \text{ GW/m}^2$ , 100 cycles; (d) W-K,  $0.44 \text{ GW/m}^2$ , 1000 cycles. Moderate-magnification: (e) W-K,  $0.44 \text{ GW/m}^2$ , 100 cycles; (f) W-K,  $0.44 \text{ GW/m}^2$ , 1000 cycles.



thermal shock tests for the different tungsten grades. The cracking thresholds for PW and W-K were 0.44–0.66 GW/m<sup>2</sup>, higher than 0–0.22 GW/m<sup>2</sup> of WL10 [11–13]. WL10 exhibited the lowest cracking threshold caused by the low thermal conductivity and La<sub>2</sub>O<sub>3</sub> particles distributed at the grain boundaries. Lower thermal conductivity naturally resulted in higher surface temperature and thermal stresses. The La<sub>2</sub>O<sub>3</sub> particles distributed at the grain boundaries would inhibit the grain boundary movement, increase the strength of grain boundary and facilitate the brittle cleavage fracture, plus, these coarse hard particles introduce stress concentrations at the grain boundaries and tend to localize strains and cracking near them. By contrast, W-K alloy presented the best thermal shock resistance considering the fact that the elongated grains aligned perpendicular to the heat flux direction. The best thermal shock resistance of W-K can be attributed to the moderate thermal conductivity, lower surface temperature, and lower DBTT. More importantly, a large amount of fine potassium bubbles distributed at the grain boundaries improved the strength of grain boundaries as well and did not introduce stress concentrations or facilitate cracking. In addition, the melting threshold for WL10 was 0.66–0.88 GW/m<sup>2</sup> while both PW and W-K exhibited the melting threshold above 1.1 GW/m<sup>2</sup>, which was caused by the low melting point of La<sub>2</sub>O<sub>3</sub> particles [11–13].

### 3.3. Thermal fatigue test

According to the different performance in thermal shock loads, thermal fatigue tests were performed on PW, WL10 and W-K samples with an absorbed power density of 0.25 GW/m<sup>2</sup>, 0.17 GW/m<sup>2</sup> and 0.44 GW/m<sup>2</sup>, respectively. The surface temperature evolution is displayed in Fig. 1. Fig. 7 shows the results after thermal fatigue tests for the different tungsten grades. For PW, the specimens endured 100 cycles without showing any signs of cracking. As the cycles increased to 1000, cracks with width of 8 μm were detected as shown in Figs. 8(a) and 9(a). As for WL10, no deterioration except slightly roughening was observed after 1 cycle, which indicated the cracking threshold for WL10 was in the range of 0.17–0.22 GW/m<sup>2</sup>. After 100 cycles, the cracks with the maximal width of 3 μm appeared. After 1000 cycles, the maximal crack width increased up to 9 μm (see Figs. 8(b) and 9(b)). In addition,

La<sub>2</sub>O<sub>3</sub> particles dissociated from the tungsten matrix in the side-wall of cracks (Fig. 9(b)). In the case of the W-K alloy, after 1 cycle, the surface kept its original morphology without any damage. As the cycles increased to 100, obvious surface roughening was detected on the whole loaded area, which was caused by the fact that deformation is accumulated as the time scale is too short for a full relaxation of the compressive stresses during cycling. But less deformation accumulation occurred for PW and WL10 during thermal fatigue tests due to the lower absorbed power densities (0.25 GW/m<sup>2</sup> for PW, 0.17 GW/m<sup>2</sup> for WL10 and 0.44 GW/m<sup>2</sup> for W-K) and higher strength (1068 MPa for PW, 1312 MPa for WL10 and 856 MPa for W-K) as well as cracks on WL10 facilitating the stress relief. But the formation of the dark region visible in Fig. 9(c) was not absolutely clear. Furthermore, it is noteworthy that the roughening occurred only in certain areas rather than throughout the loaded area after 1000 cycles (Figs. 8(d) and 9(d)), which could be associated with some inhomogeneities in the W-K alloy. We will figure out this phenomenon in the future. Besides, in the smooth area, grain boundaries were observed and the grain size was around 10 μm, which is thought to be related to the recrystallization of the tungsten matrix. But it is exciting that no cracks emerged after 1000 cycles.

In comparison with PW, WL10 displayed worse thermal and fatigue resistance while W-K exhibited opposite results, which can be attributed to a moderate number of coarse La<sub>2</sub>O<sub>3</sub> particles and a large amounts of fine potassium bubbles at grain boundaries. La<sub>2</sub>O<sub>3</sub> particles are mainly distributed at grain boundaries, which are prone to decohesion and fracture during loading, especially for the coarse particles inducing a greater severe stress/strain concentration and they are also more likely to break because of the fracture strength of particles scales inversely with particle size. But for the W-K alloy, the presence of fine potassium bubbles at the grain boundaries improved the strength of grain boundaries as well and did not introduce stress concentrations or facilitate cracking. Since the W-K materials had the lowest bend strength but the WL10 alloy had the lowest melting threshold, perhaps thermal shock and fatigue resistance can be improved by using a Y<sub>2</sub>O<sub>3</sub> or TiC dispersion-strengthened tungsten with ultra fine grains and optimized particles (reduced in size and predominantly dispersed within grains). Strength and melting threshold are

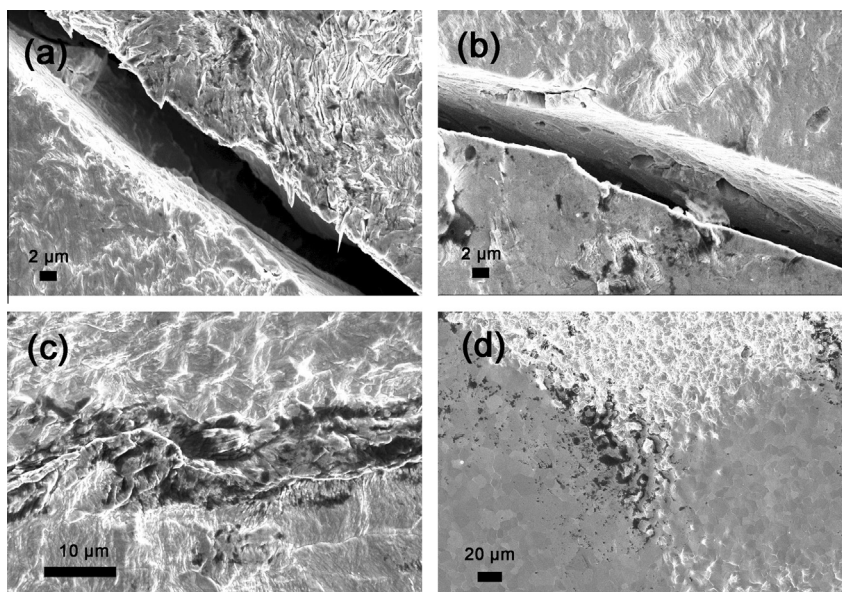


**Fig. 9.** High-magnification SEM images of tungsten grades after thermal fatigue tests: (a) PW, 0.25 GW/m<sup>2</sup>, 1000 cycles; (b) WL10, 0.17 GW/m<sup>2</sup>, 1000 cycles; (c) W-K, 0.44 GW/m<sup>2</sup>, 100 cycles; (d) W-K, 0.44 GW/m<sup>2</sup>, 1000 cycles.

meaningful parameters for tungsten grades selected as PFM in fusion reactor. Low strength resulted in surface roughening: the hot surface expanded and generated compressive stresses which could cause deformation of tungsten at high temperature if the thermal stresses exceeded the yield strength [14]. A low melting threshold can result in plasma contamination via particle release due to surface melting of tungsten. Furthermore, evaporation of low-melting particles, such as  $\text{La}_2\text{O}_3$ , can aggravate crack formation as reported in Ref. [12,15]. Therefore,  $\text{Y}_2\text{O}_3$  or TiC dispersion-strengthened tungsten might exhibit high strength and melting threshold simultaneously.

#### 4. Conclusions

Thermal shock and fatigue tests were performed on specimens cut from rolled pure W (PW) and W–1 wt%  $\text{La}_2\text{O}_3$  (WL10) as well as swaged + rolled W doped with 70–75 ppm K (W-K) bulk specimens in an electron beam facility. In comparison with PW, WL10 displayed lower thermal and fatigue resistance while W-K exhibited better properties, which is attributed to the differences in thermal–mechanical properties of the three tungsten materials and the size and number density of coarse  $\text{La}_2\text{O}_3$  particles and potassium bubbles. A moderate quantity of ellipsoid  $\text{La}_2\text{O}_3$  particles with an aspect ratio of roughly 1.5–3, length of 1–4  $\mu\text{m}$  and number density (per unit area) of  $10^8 \text{ m}^{-2}$  were distributed at grain boundaries for WL10, while an appreciable number of potassium bubbles with sizes of 50–200 nm and number density (per unit area) of  $10^{13} \text{ m}^{-2}$  were distributed at the grain boundaries for W-K. Furthermore,  $\text{La}_2\text{O}_3$  may not be suitable for ideal PFM considering it is melting issues and TiC or  $\text{Y}_2\text{O}_3$  may be preferred. TiC or  $\text{Y}_2\text{O}_3$  can improve the strength of tungsten alloys and bear higher

temperature simultaneously. Besides, W-K alloy is also a choice for PFM if the surface roughening issue can be solved.

#### Acknowledgement

The authors gratefully acknowledge the financial support of ITER-National Magnetic Confinement Fusion Program (2014GB123000).

#### References

- [1] V. Kotov, A. Litnovsky, A.S. Kukushkin, D. Reiter, A. Kirschner, J. Nucl. Mater. 390 (2009) 528–531.
- [2] A. Cardella, H. Gorenflo, A. Lodato, K. Ioki, R. Raffray, J. Nucl. Mater. 283 (2000) 1105–1110.
- [3] M. Merola, M. Rödiger, J. Linke, R. Duwe, G. Vieider, J. Nucl. Mater. 258 (1998) 653–657.
- [4] V.A. Makhilaj, I.E. Garkusha, S.V. Malykhin, A.T. Pugachov, I. Landman, J. Linke, S. Pestchanyi, V.V. Chebotarev, V.I. Tereshin, Phys. Scr. 2009 (2009) 14060.
- [5] M. Mabuchi, K. Okamoto, N. Saito, T. Asahina, T. Igarashi, Mater. Sci. Eng. A 237 (1997) 241–249.
- [6] Y. Kim, K.H. Lee, E. Kim, D. Cheong, S.H. Hong, Int. J. Refract. Metal Hard Mater. 27 (2009) 842–846.
- [7] R. Liu, X.P. Wang, T. Hao, C.S. Liu, Q.F. Fang, J. Nucl. Mater. 450 (2014) 69–74.
- [8] M. Faleschini, H. Kreuzer, D. Kiener, R. Pippan, J. Nucl. Mater. 367 (2007) 800–805.
- [9] Q. Yan, X. Zhang, T. Wang, C. Yang, C. Ge, J. Nucl. Mater. 442 (2013) S233–S236.
- [10] Q. Wei, L.J. Kecskes, Mater. Sci. Eng. A 491 (2008) 62–69.
- [11] X. Zhang, Q. Yan, J. Nucl. Mater. 444 (2014) 428–434.
- [12] X. Zhang, Q. Yan, J. Nucl. Mater. 451 (2014) 283–291.
- [13] X. Zhang, Q. Yan, S. Lang, M. Xia, C. Ge, J. Nucl. Mater. 452 (1–3) (2014) 257–264.
- [14] I. Uytendhouwen, M. Decréton, T. Hirai, J. Linke, G. Pintsuk, G. Van Oost, J. Nucl. Mater. 363 (2007) 1099–1103.
- [15] T. Hirai, W. Kühnlein, J. Linke, G. Sergienko, Dynamic erosion of plasma facing materials under ITER relevant thermal shock loads in the electron beam facility, JUDITH, in: 20th IAEA Fusion Energy Conference, 2004, FT/P1-20.